research papers

X-ray and neutron diffraction studies of the non-linear optical compounds MBANP and MBADNP at 20 K: charge-density and hydrogen-bonding analyses

Jacqueline M. Cole,[a,b]*† **Andrés E. Goeta,**[b] **Judith A. K. Howard**[b] **and Garry J. McIntyre**[a]

[a]Institut Laue Langevin, BP 156, 38042 Grenoble Cedex 9, France, and [b]Department of Chemistry, University of Durham, South Road, Durham DH1 3LE, UK

† Present address: Department of Chemistry, University of Cambridge, Lensfield Road, Cambridge CB2 1EW, UK

Correspondence e-mail: jmc61@cam.ac.uk

Neutron-diffraction studies of the compounds 5-nitro-2-{[1-phenylethyl]amino}pyridine (methylbenzylaminonitro-pyridine, hereafter MBANP) and 3,5-dinitro-2-{[1-phenyl-ethyl]amino}pyridine (methylbenzylaminodinitropyridine, hereafter MBADNP) are presented, and a charge-density study of the latter is reported. The studies were conducted in order to relate the structural attributes of these materials to their physical properties. MBANP exhibits a second-harmonic generation (SHG) output, $\chi^{(2)}$, over eight times higher than that of MBADNP, despite their very similar molecular characteristics and the seemingly more SHG-favourable molecular features present in MBADNP. The neutron-diffraction studies show that intramolecular hydrogen bonding is responsible for this apparent discrepancy. The charge-density study on MBADNP confirms this and reveals that the pyridine group is the principal moiety responsible for the SHG effect on the molecular scale. Moreover, the strong intra-molecular hydrogen bond present in MBADNP is proven to result from an electrostatic interaction. The dipole moment of MBADNP is also deduced from the charge-density study.

1. Introduction

Organic non-linear optical (NLO) materials have shown great promise in the optoelectronic and telecommunication industries over recent years (Fejer, 1994; Zyss, 1994; Burland, 1994; Long, 1995). In particular, measurements of the second-order NLO effect, second-harmonic generation (SHG), on certain organic NLO compounds have already produced results that far exceed those obtained from all known inorganic NLO alternatives (Chemla & Zyss, 1987) such as $LiNbO_3$. Organic materials also have much faster optical response times, significantly higher optical thresholds and much greater versatility in molecular design compared with their inorganic counterparts. Thus, there is much impetus to design and understand organic compounds for SHG applications.

The level of SHG output depends inherently on the molecular and supramolecular nature of a given compound. On a molecular scale, β [the first non-linear molecular hyperpolarizability coefficient of a power series of **p**, the total polarization of a molecule, as a function of **E**, the applied electric field (Chemla & Zyss, 1987)] is a measure of the SHG potential and is maximized when the extent of charge transfer across a molecule is large (Davydov et al., 1970; Oudar, 1977; Oudar & Zyss, 1982; Lalama & Garito, 1979; Albrecht & Morell, 1979). This occurs when the molecule contains strong electron donors and acceptors, separated by an extended π-conjugated

'electronic bridge'. The more delocalized the π-electron density, the more effective the molecular charge transfer as deduced by bond-length alternation considerations (Gorman & Marder, 1993; Marder & Perry, 1993). The incorporation of one or more aromatic (Davydov et al., 1970) and/or 'reduced' aromatic (Docherty et al., 1985; Jen et al., 1993; Cheng et al., 1991) moieties has been shown to be important in optimizing this level of delocalization. The presence of these rings is also often important for providing relevant π–π* transitions for the SHG effect.

On a supramolecular scale, the macroscopic second-order susceptibility to polarization $\chi^{(2)}$ [the first non-linear coefficient of a power series of **P**, the total polarization of a medium, as a function of **E**, the applied electric field (Chemla & Zyss, 1987)] is a measure of the SHG activity of a compound. The value of $\chi^{(2)}$ is greater than zero only if a molecule packs in a non-centrosymmetric arrangement, owing to the third-rank tensorial nature of the SHG effect (Cady, 1946). In a crystal, the relative orientation and proximity of one molecule with respect to another controls the ease with which charge transfer will propagate through the lattice. The natures of the crystal packing, local crystal-field effects and intermolecular interactions therefore highly influence the SHG effect, as has been shown previously (Sarma et al., 1997; Cole, 1997; Cole et al., 2001). For practical application, the level of phase-matching ability (Armstrong et al., 1962; Franken & Ward, 1963) of a material is very important. There exists an inherent relationship between crystal symmetry and the phase-matching angle, θ_{PM} (Oudar & Zyss, 1982), by which the phase-matching ability is measured. In the monoclinic crystal system (to which both subject crystal structures belong), θ_{PM} is defined as the angle between the charge-transfer axis of the molecule and the crystallographic screw axis that generates the herringbone structure, and its optimal value is 54.74° (Oudar & Zyss, 1982).

We became interested in discovering why the well-known SHG-active material MBANP (Fig. 1a) (Twieg & Dirk, 1986; Kondo et al., 1988, 1989; Bailey et al., 1993) exhibits a macroscopic SHG output of 25 times that of urea, the standard reference sample (Twieg et al., 1982; Twieg & Dirk, 1986), whereas the meta substitution of an NO$_2$ group on the pyridine ring to form MBADNP (Fig. 1b) yields an SHG output of only three times that of urea (Cole et al., 1997), despite the fact that this substitution ostensibly affords more structurally favourable prospects for SHG. Specifically, (a) the meta-substituted NO$_2$ group in MBADNP provides better molecular charge-transfer possibilities than MBANP; (b) substitution at the meta position of the pyridine ring would ensure a decrease in the delocalization energy of the aromatic ring, and such 'reduced' aromaticity has been shown to improve SHG properties (Jen et al., 1993; Cheng et al., 1993); (c) the extra NO$_2$ group affords greater availability of hydrogen-bond donors and acceptors in MBADNP compared with MBANP; (d) both MBANP and MBADNP crystallize in the same space group ($P2_1$); and (e) the phase-matching angle, θ_{PM}, in MBADNP (63°; Cole et al., 1997) is closer to the optimal value [54.7° for monoclinic crystal systems (Oudar & Zyss, 1982)] than that in MBANP (34°; Bailey et al., 1991).

A comparative inspection of the crystal structures of MBANP and MBADNP derived by X-ray diffraction (Twieg & Dirk, 1986; Kondo et al., 1988; Cole et al., 1997) revealed that MBADNP packs in a less favourable layer-like arrangement than MBANP. We suspected that this factor could be partly responsible for the apparent discrepancy, especially since the X-ray diffraction results indicated that hydrogen bonding appears to dominate the three-dimensional arrangement of each compound. A detailed evaluation of the hydrogen bonding using neutron diffraction was therefore conducted in order to resolve this discrepancy. In addition, a charge-density study of MBADNP was performed in order to investigate the nature of the molecular polarization, especially in the vicinity of the meta-NO$_2$ substitution.

2. Experimental

2.1. Single-crystal neutron-diffraction measurements

All neutron-diffraction measurements on both MBANP and MBADNP were carried out using the four-circle diffractometer D9 at the Institut Laue Langevin (ILL), Grenoble, France. In each case, indexing and subsequent data collection were carried out at 20.0 (1) K using Cu(220) monochromated neutron radiation [λ = 0.8372 (1) Å]. Half-wavelength contamination was removed with an erbium filter. The low temperature, employed to minimize possible diminution of scattering owing to thermal effects, was maintained using an Air Products 512 Displex (Archer & Lehmann, 1986). Data were collected according to an ω-$x\theta$ scanning procedure, with x chosen to keep the reflection in the middle of the detector aperture and with a scan width, $\Delta\omega$, which was roughly twice the full width of the peak at background level. A standard reflection, measured every 50 reflections, showed no variation in intensity. Data were reduced to integrated intensities using a local program (Wilkinson et al., 1988) and Lorentz corrections were applied. Absorption corrections were then made by Gaussian integration (Coppens et al., 1965). Each data set was merged and the positional and anisotropic displacement parameters for all atoms in each structure were refined by full-matrix least-squares refinement using SHELXL93 (Sheldrick, 1993). A summary of crystal, data collection and independent-atom model (IAM) refinement parameters for each structure is given in Table 1.
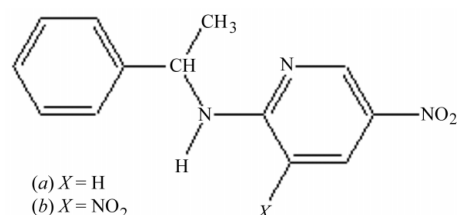
Figure 1
Schematic chemical diagrams of (a) MBANP and (b) MBADNP.

Table 1
Experimental details.

	MBANP (neutron)	MBADNP (neutron)	MBADNP (X-ray)
Crystal data			
Chemical formula	$C_{13}H_{13}N_3O_2$	$C_{13}H_{12}N_4O_4$	$C_{13}H_{12}N_4O_4$
Chemical formula weight	243	288	288.27
Cell setting, space group	Monoclinic, $P2_1$	Monoclinic, $P2_1$	Monoclinic, $P2_1$
a, b, c (Å)	5.3260 (6), 6.301 (1), 17.673 (4)†	8.3467 (8), 8.5673 (8), 8.8999 (8)†	8.352 (3), 8.570 (3), 8.909 (4)
α (°)	90	90	90
β (°)	93.42 (1)†	93.954 (8)†	93.98 (2)†
γ (°)	90	90	90
V (Å^3)	589.8 (2)	636.1 (4)	636.1 (4)
Z	2	2	2
D_x (Mg m^{-3})	1.368	1.504	1.505
Radiation type	Neutron (steady-state reactor source)	Neutron (steady-state reactor source)	Mo $K\alpha$ (rotating anode source)
No. of reflections for cell parameters	4	4	4
θ range (°)	10–12	10–12	10–12
μ (mm^{-1})	0.1582	0.1407	0.115
Temperature (K)	20.0 (1)	20.0 (1)	20.0 (2)
Crystal form, colour	Rectangle, yellow	Hexagonal prism, yellow	Block, yellow
Crystal size (mm)	$4.3 \times 2.0 \times 1.0$	$3.0 \times 2.5 \times 1.0$	$0.30 \times 0.26 \times 0.20$
Data collection			
Diffractometer	D9 at ILL, Grenoble, France	D9 at ILL, Grenoble, France	Fddd cryodiffractometer at Durham, UK
Data collection method	ω–x–θ scans	ω–x–2θ scans	ω scans
Absorption correction	Integration	Integration	Integration
T_{min}	0.7263	0.7569	0.9774
T_{max}	0.8574	0.8802	0.9822
No. of measured, independent and observed reflections	4116, 2805, 2619	3755, 3401, 3267	16427, 7873, 7613
Criterion for observed reflections	$I > 2\sigma(I)$	$I > 2\sigma(I)$	$I > 2\sigma(I)$
R_{int}	0.0384	0.0283	0.0203
θ_{max} (°)	46.46	46.56	39.97
Range of h, k, l	$-9 \rightarrow h \rightarrow 9$	$0 \rightarrow h \rightarrow 14$	$-15 \rightarrow h \rightarrow 15$
	$-10 \rightarrow k \rightarrow 2$	$-10 \rightarrow k \rightarrow 14$	$-15 \rightarrow k \rightarrow 15$
	$-22 \rightarrow l \rightarrow 21$	$-15 \rightarrow l \rightarrow 13$	$-16 \rightarrow l \rightarrow 16$
No. and frequency of standard reflections	1 every 50 reflections	1 every 50 reflections	4 every 146 reflections
Refinement			
Refinement on	F^2	F^2	F^2
$R[F^2>2\sigma(F^2)]$, $wR(F^2)$, S	0.0732, 0.1051, 2.632	0.0291, 0.0464, 1.484	0.0333, 0.1146, 0.989
No. of reflections and parameters used in refinement	2799, 280	3397, 298	7873, 238
H-atom treatment	All H-atom parameters refined	All H-atom parameters refined	All H-atom parameters refined
Weighting scheme	$w = 1/[\sigma^2(F_o^2)]$	$w = 1/[\sigma^2(F_o^2)]$	$w = 1/[\sigma^2(F_o^2) + (0.1P)^2]$ where $P = (F_o^2 + 2F_c^2)/3$
$(\Delta/\sigma)_{max}$	0	0	0.001
$(\Delta/\sigma)_{max}$	-0.004	0.000	0
$\Delta\rho_{max}$, $\Delta\rho_{min}$ (fm Å^{-3}, e Å^{-3})	1.795, -1.868	0.815, -0.909	0.61, -0.265

Computer programs used: *MAD* (Barthelemy, 1984), *RAFD9* (local program), *RACER* (Wilkinson *et al.,* 1988), *SHELXS*86 (Sheldrick, 1990), *SHELXL*93 (Sheldrick, 1993), *COLL5N* (Lehmann & Wilson, 1987), *SHELXS*97 (Sheldrick, 1997). † Although these neutron-derived cell parameters were used for data collection, 20 K X-ray-derived cell parameters $a = 5.321$ (1) Å, $b = 6.293$ (1) Å, $c = 17.650$ (4) Å, $\beta = 93.65$ (3)° (MBANP) and $a = 8.352$ (3) Å, $b = 8.570$ (3) Å, $c = 8.909$ (4) Å, $\beta = 93.98$ (2)° (MBADNP) determined using the Fddd cryodiffractometer in Durham (Copley *et al.,* 1997) were used in all calculation, correction and refinement procedures since they are deemed more accurate than neutron-derived values. Moreover, the neutron wavelength's estimated standard deviation was not used in the calculation of the neutron-derived cell parameters.

2.2. Single-crystal X-ray diffraction measurements for charge-density study

A $0.30 \times 0.26 \times 0.20$ mm crystal of MBADNP was mounted on the Fddd cryodiffractometer at Durham, UK (Copley *et al.*, 1997). This device is equipped with an Mo rotating anode ($\lambda = 0.71073$ Å), which enables data collection of weak or small samples, and incorporates sub-liquid-nitrogen temperature measurement capabilities (down to 10 K) using an Air Products 512 Displex (Archer & Lehmann, 1986). All measurements were made at 20.0 (2) K. The very

low temperature of data collection is important for yielding the maximum possible intensity of atomic scattering, which is of paramount concern in charge-density studies, particularly since the high-angle (weaker) data represent mostly the atomic scattering from the core electrons. The associated increase in the overall number of observed reflections is also important for ensuring an adequate data-to-parameter ratio for a multipolar refinement to be viable.

Data were collected in shells covering the range $2 \leq \theta \leq 40°$ ($-15 \leq h \leq 15$, $-15 \leq k \leq 15$, $-16 \leq l \leq 16$) in bisecting

mode, using ω scans with a constant scan width of $1.4°$. A total of 16 462 reflections were collected to $(\sin\theta/\lambda)_{max} = 0.904$ Å^{-1} over a period of one month. Four standard reflections, measured every 146 reflections, showed no variation in intensity throughout the experiment. The resulting data were reduced using *COLL5N* (Lehmann & Wilson, 1987) and corrected for absorption using Gaussian integration (Coppens *et al.*, 1965). Some φ-scan measurements, which had been performed for several reflections during the experiment, confirmed that the absorption correction was satisfactory. The corrected data were scaled and merged using the *DREAM* suite of programs (Blessing, 1986). In order to obtain a starting model for a multipolar refinement, a conventional IAM refinement of the positional and anisotropic displacement parameters of all non-H atoms and positional and isotropic displacement parameters for the H atoms was undertaken using *SHELXL*93 (Sheldrick, 1993), employing full-matrix least-squares procedures. The absolute structure could not be determined reliably from this experiment; however, it was known *a priori* to exist in the *R*-configuration, since *R*-α-methylbenzylamine was one of the starting materials and this stereochemistry was retained through to the product. A summary of crystal, data collection and refinement parameters is given in Table 1.

2.3. The multipolar refinement

Multipolar refinement was applied to the data starting from the IAM model and using the *XD* suite of programs (Koritsanszky *et al.*, 1994). These employ spherical and aspherical atom-centred density functions to model the total electron density of the structure in the following manner:

$$\rho_{atom}(\mathbf{r}) = P_c\rho_{core}(r) + P_v\kappa^3\rho_{valence}(\kappa r)$$
$$+ \sum_{l=0}^{l_{max}} \kappa'^3 R_l(\kappa'r) \sum_{m=0}^{l} P_{lm\pm}d_{lm\pm}(\mathbf{r}/r),$$

where ρ_{core} and $\rho_{valence}$ are Hartree–Fock spherical core and valence densities, respectively; P_c and P_v are the populations of the core and valence shells, respectively; $P_{lm\pm}$ are the multipolar population parameters of each normalized associated Legendre function, $d_{lm\pm}$ of order l; m corresponds to the orientation of l; κ and κ' are the contraction and expansion coefficients for the spherical and multipolar valence densities, respectively; and $R_l(\kappa'r)$ represents the Slater-type radial functions as defined by

$$R_l(r) = \frac{\xi^{n_l+3}}{(n_l+2)!}(r)^{n(l)}\exp(-\xi r),$$

where $n > 1$ is required to satisfy Poisson's electrostatic requirements (Stewart, 1977) and ξ is the energy-optimized single Slater exponent for the electron subshells of isolated atoms: $\xi = (Z-\sigma)/n$, (Z = charge, σ = screening constant, n = principal quantum number), and for each element it is taken from tabulated values (Clementi & Raimondi, 1963) and modified by the variable κ', such that $\xi' = \kappa'\xi$ (Hansen & Coppens, 1978).

Once the refinement of the initial parameters had converged, a κ parameter for each atom was introduced. All κ values relating to non-H atoms were initially set at 1.0 and refined to 0.968 (3) (C), 0.978 (4) (N) and 0.976 (2) (O), whereas the κ value for H atoms was fixed to the Stewart–Davidson–Simpson (hereafter SDS) value of 1.16 (Stewart *et al.*, 1965). Throughout the refinement, an electroneutrality constraint was applied in order to ensure an overall null-balanced molecular charge. The H coordinates and anisotropic displacement parameters in the *XD* refinement were then replaced by the refined neutron-derived values; the X-ray and neutron non-H coordinates were identical within the statistical uncertainty, and so the X-ray values were retained for these parameters. Whilst the neutron-derived H atomic coordinates directly replaced the X-ray values, the neutron-derived H anisotropic displacement parameters were scaled with respect to the X-ray values before substitution. The scaling parameter was determined from the difference between the X-ray and neutron non-H anisotropic displacement parameters (U_X^{ij} and U_N^{ij}, respectively) according to the following weighted formula by Blessing (1995):

$$U_X^{ij} = U_N^{ij} + \Delta U^{ij},$$

where

$$\Delta U^{ij} = \sum_a \left(\sum_a wU_X^{ij} - \sum_a wU_N^{ij} \right) / \sum_a w$$

and

$$w = 1/\sigma^2$$

where

$$\sigma = \sigma(U_X^{ij} - U_N^{ij}) = [\sigma^2(U_X^{ij}) + \sigma^2(U_N^{ij})]^{1/2}.$$

The scaling parameter, ΔU^{ij}, was small (4.99×10^{-4}), indicating that there is good agreement between the displacement parameters derived from the two diffraction experiments at 20 K. The scaling parameter was simply added to all H-atom anisotropic displacement parameters to give the new values for substitution. The resulting H atomic coordinates and anisotropic displacement parameters were fixed in all subsequent refinements.

Multipolar terms were then introduced, starting with the refinement of monopolar (P_v) and dipolar (bond-directed for H atoms) populations on all atoms. Once these had converged, quadrupolar and octopolar terms were refined for all non-H atoms. Refinement at the hexadecapolar level for all non-H atoms was also attempted. However, the population of these functions was negligible (the maximum hexadecapolar function population was less than twice its estimated standard deviation) and so these functions were not used in the final refinements.

An attempt was then made to subdivide the κ parameters into six values that reflected the different bonding hybridizations of each elemental atom type. This did not improve the fit and thus was not employed. Different κ' parameters for each elemental type were also introduced at this point, but refine-

Table 2
Bond lengths (Å) for the 20 K neutron structures of MBANP and MBADNP.

Bond	MBANP	MBADNP	Bond	MBANP	MBADNP
O(1)—N(3)	1.226 (4)	1.239 (1)	C(3)—H(3)	1.072 (8)	1.089 (2)
O(2)—N(3)	1.237 (3)	1.223 (1)	C(4)—C(5)	1.385 (4)	1.400 (1)
O(3)—N(4)	–	1.229 (1)	C(4)—H(4)	1.080 (7)	1.090 (2)
O(4)—N(4)	–	1.234 (1)	C(5)—C(6)	1.399 (4)	1.395 (1)
N(1)—C(9)	1.354 (3)	1.338 (1)	C(5)—H(5)	1.084 (6)	1.084 (2)
N(1)—C(7)	1.455 (3)	1.473 (1)	C(6)—H(6)	1.087 (6)	1.086 (2)
N(1)—H(1N)	1.019 (5)	1.013 (2)	C(7)—C(8)	1.532 (4)	1.532 (1)
N(2)—C(13)	1.337 (3)	1.321 (1)	C(7)—H(7)	1.106 (6)	1.101 (2)
N(2)—C(9)	1.354 (3)	1.361 (1)	C(8)—H(8A)	1.085 (8)	1.094 (3)
N(3)—C(10)	–	1.454 (1)	C(8)—H(8B)	1.076 (8)	1.098 (2)
N(3)—C(12)	1.443 (3)	–	C(8)—H(8C)	1.080 (7)	1.093 (2)
N(4)—C(12)	–	1.447 (1)	C(9)—C(10)	1.418 (4)	1.437 (1)
C(1)—C(2)	1.394 (4)	1.397 (1)	C(10)—C(11)	1.369 (4)	1.381 (1)
C(1)—C(6)	1.404 (4)	1.403 (1)	C(10)—H(10)	1.073 (7)	–
C(1)—C(7)	1.522 (4)	1.521 (1)	C(11)—C(12)	1.409 (4)	1.387 (1)
C(2)—C(3)	1.388 (4)	1.401 (1)	C(11)—H(11)	1.082 (7)	1.084 (2)
C(2)—H(2)	1.089 (6)	1.089 (2)	C(12)—C(13)	1.386 (4)	1.398 (1)
C(3)—C(4)	1.396 (4)	1.395 (1)	C(13)—H(13)	1.088 (7)	1.090 (2)

Table 3
Selected bond angles (°) for the 20 K neutron structures of MBANP and MBADNP.

Angle	MBANP	MBADNP	Angle	MBANP	MBADNP
C(7)—N(1)—C(9)	123.4 (2)	123.85 (6)	C(6)—C(1)—C(7)	121.4 (2)	118.93 (8)
C(9)—N(1)—H(1N)	117.2 (4)	117.0 (1)	N(1)—C(7)—C(1)	112.9 (2)	107.46 (7)
C(7)—N(1)—H(1N)	118.3 (4)	118.2 (1)	N(1)—C(7)—C(8)	108.3 (2)	110.40 (7)
C(9)—N(2)—C(13)	117.6 (2)	119.59 (7)	C(1)—C(7)—C(8)	109.2 (2)	114.39 (7)
O(1)—N(3)—O(2)	123.1 (3)	123.21 (9)	N(1)—C(9)—N(2)	117.8 (2)	116.87 (7)
O(1)—N(3)—C(10)	–	118.30 (8)	N(1)—C(9)—C(10)	119.5 (2)	123.57 (7)
O(1)—N(3)—C(12)	119.0 (2)	–	C(9)—C(10)—N(3)	–	122.87 (7)
O(2)—N(3)—C(10)	–	118.47 (8)	C(11)—C(10)—N(3)	–	116.60 (7)
O(2)—N(3)—C(12)	117.9 (2)	–	C(11)—C(12)—N(3)	120.0 (2)	–
O(3)—N(4)—O(4)	–	123.82 (8)	C(11)—C(12)—N(4)	–	119.70 (7)
O(3)—N(4)—C(12)	–	117.98 (7)	C(13)—C(12)—N(3)	120.0 (2)	–
O(4)—N(4)—C(12)	–	118.20 (7)	C(13)—C(12)—N(4)	–	120.22 (7)
C(2)—C(1)—C(7)	119.1 (2)	122.47 (8)			

ment led to notably poorer statistics. This was not unexpected since it is well known that these are very sensitive parameters (Volkov *et al.*, 2001) and the data-to-parameter ratio was only ~7 without these extra parameters. κ' values for all non-H and H atoms were therefore fixed to 1 and 1.16, respectively.

Care was taken throughout the refinement with regard to the arbitrariness in the refined sums of the odd-order multipole terms – a potential problem in all non-centrosymmetric structures (Terpstra *et al.*, 1993; El Haouzi *et al.*, 1996). Any such problem was circumvented by employing the chemically reasonable assumption that the bonding deformations for each specific element type are equivalent.

3. Results and discussion

3.1. Hydrogen-bonding studies of MBANP and MBADNP

A 50% probability thermal ellipsoid plot of each neutron-diffraction-derived structure is given in Figs. 2 and 3. Associated bond lengths are given in Table 2 and selected bond

angles are given in Table 3. Fractional coordinates and atomic displacement parameters are deposited[1]

The three-dimensional crystal packing and the extent of hydrogen bonding present in MBANP and MBADNP were compared. In both structures, all non-bonded contacts detected previously by X-ray diffraction are also present here and are stronger than those determined using X-ray diffraction. Moreover, in MBADNP, five further contacts were located by neutron diffraction. This is expected since X—H distances obtained using X-ray diffraction appear artificially shorter than their 'true' neutron values; hence, X-ray-derived $X \cdots$H distances appear longer than those derived from neutron diffraction studies.

These results show that MBANP possesses one primary intermolecular hydrogen bond, N(1)—H(1N)$\cdots$O(2) [2.009 (7) Å, symmetry code $x - 1$, $y - 1$, z], one secondary intermolecular hydrogen bond, C(10)—H(10)$\cdots$O(1) [2.488 (7) Å, symmetry code $2 - x$, $y - \frac{1}{2}$, $1 - z$], and two intramolecular contacts, C(11)—H(11)$\cdots$O(1) [2.464 (8) Å] and C(13)—H(13)$\cdots$O(2) [2.398 (8) Å], of intermediate strength judging from their distances. This arrangement uses all possible classical hydrogen-bond donors and acceptors. Furthermore, the planes stack almost directly on top of each other (see Fig. 4) with an interplanar spacing of 6.29 (2) Å along the b direction and only 5.32 (2) Å along the a direction. This very efficient and close layer-like packing facilitates suitable electronic (δ^+/δ^-) interactions between molecules, which is ideal for effective propagation of the SHG phenomenon throughout the solid as is evidenced by comparing the relationship between β and $\chi^{(2)}$ via local field factors, f, at the fundamental and second-harmonic frequencies ω and 2ω, respectively (Oudar & Zyss, 1982; Burland *et al.*, 1994):

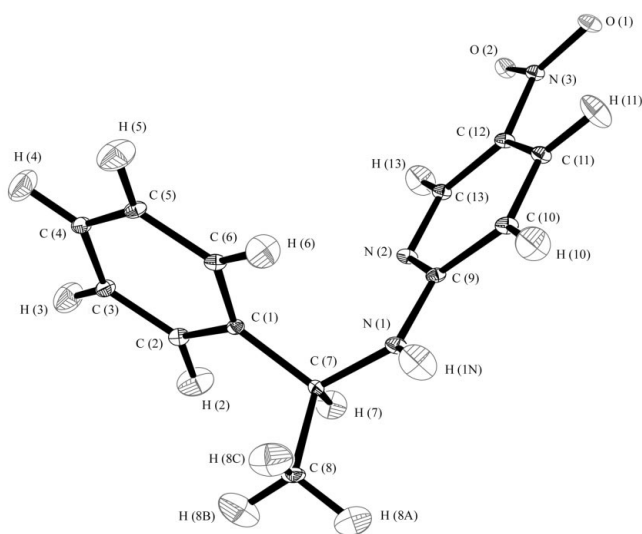$$\chi^2 = N f_I^{2\omega} f_J^{\omega} f_K^{\omega} \langle \beta_{ijk} \rangle_{IJK},$$

where $\langle \beta_{ijk} \rangle_{IJK}$ is the expectation value of β, *i.e.* the weighted sum of β over all orientations of the molecule, ijk, with respect to the crystal frame, IJK, and N is the number of molecules per unit volume.

MBADNP, on the other hand, contains five intramolecular close contacts and five intermolecular ones. Four of the intramolecular non-bonded contacts [O(1)$\cdots$N(1) = 2.684 (2), C(2)—H(2)$\cdots$C(8) = 2.528 (3), C(7)—H(7)$\cdots$N(2) = 2.447 (2), C(11)—H(11)$\cdots$O(2) = 2.359 (3) Å] appear to be intermediate to weak in strength. The fifth intramolecular

non-bonded contact, N(1)—H(1N)···O(1) [1.971 (3) Å], however, is notably short and appears to be responsible for the twist in the chain between the two rings that is induced as the molecule adjusts to try to accommodate it. This twist precludes an ideal herringbone formation in the three-dimensional lattice and disrupts what would otherwise be close layer-like packing (see Fig. 5). The result yields an interplanar spacing of 8.6 (2) Å along the b direction, which is noticeably larger than that in MBANP. Moreover, although the interplanar spacing along the a direction in MBADNP [4.1 (2) Å] is shorter than the corresponding spacing in MBANP, the molecules in MBADNP do not lie directly side by side as in MBANP but are significantly displaced away from each other.

The intermolecular interactions are thus affected. The twist deterring the molecules from slotting over each other efficiently (in contrast to MBANP) restricts the number of possible close contacts. Not all hydrogen-bond donors and acceptors are utilized, and all of the intermolecular non-bonded contacts are of weak to intermediate strength

$[N(1)—H(1N)···O(4)$ $(x - 1,$ $y,$ $z)$ $=$ $2.316 (3),$ $C(2)—H(2)···C(4)$ $(3 - x,$ $y - \frac{1}{2},$ $- z)$ $=$ $2.627 (3),$ $C(3)—H(3)···O(1)$ $(3 - x,$ $y - \frac{1}{2},$ $- z)$ $=$ $2.562 (3),$ $C(5)—H(5)···O(3)$ $(x - 1,$ $y,$ $z + 1)$ $=$ $2.438 (4),$ $C(6)—H(6)···C(8)$ $(2 - x, \frac{1}{2} + y, - z) = 2.666 (3)$ Å].

The one strong intramolecular hydrogen bond, N(1)—H(1N)···O(1), therefore appears to form at the expense of the intermolecular interactions. Given that the resulting crystal packing of MBADNP is less optimal than that of MBANP, we believe that this, in turn, is the cause of the much lower efficiency of SHG propagation through the three-dimensional solid of MBADNP compared with MBANP. In

Figure 4
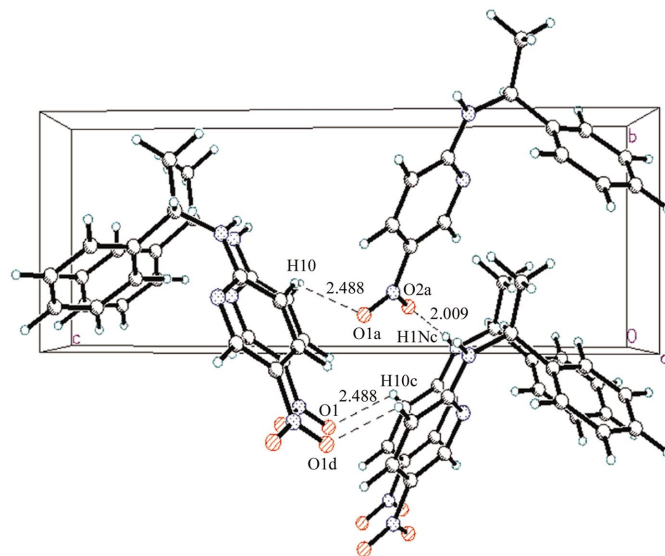The molecular packing arrangement of the 20 K neutron structure of MBANP.

Figure 2
A 50% probability thermal ellipsoid plot of the 20 K neutron structure of MBANP.
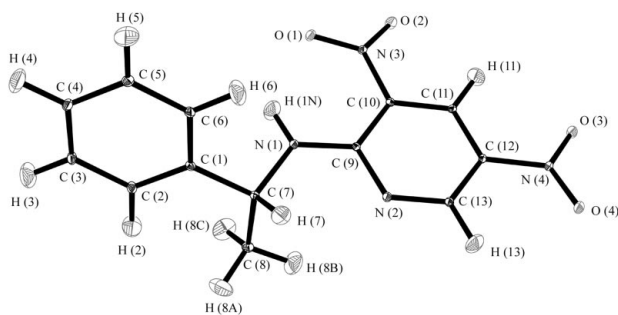
Figure 3
A 50% probability thermal ellipsoid plot of the 20 K neutron structure of MBADNP.
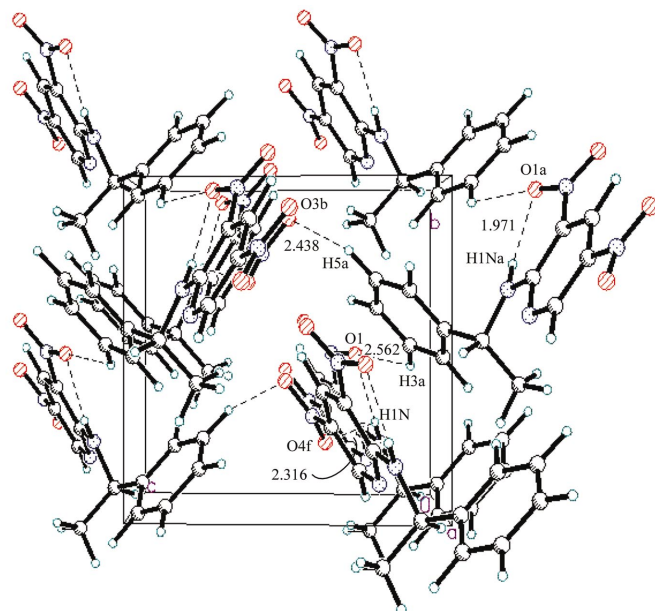
Figure 5
The molecular packing arrangement of the 20 K neutron structure of MBADNP.

Table 4
A summary of refinement parameters for the charge-density study of MBADNP.

Parameter	Value	Parameter	Value
Scale factor	0.595 (1)	Weighting scheme	$1/\sigma^2$
Criterion for observed data	$F = 2\sigma(F)$	$R_w(F)$	0.0176
$R(F)$	0.0171	$R_w(F^2)$	0.0357
$R(F^2)$	0.0300	GOF_w	1.0591
$R_{all}(F)$	0.0171	Data, parameter	3890, 552
$R_{all}(F^2)$	0.0300	$\Delta/\sigma_{(min, max)}$	$0.9 \times 10^{-9}, 0.2 \times 10^{-5}$
GOF	1.0419	$\Delta\rho_{(min, max)}$	$-0.112, 0.173$

Table 5
Pseudoatomic charges for each atom in MBADNP determined from the multipolar refinement.

Atom	Charge	Atom	Charge	Atom	Charge
O(1)	-0.18 (3)	C(4)	-0.15 (5)	H(2)	0.18 (3)
O(2)	0.01 (3)	C(5)	0.08 (6)	H(3)	0.09 (3)
O(3)	0.00 (3)	C(6)	-0.03 (5)	H(4)	0.13 (3)
O(4)	-0.10 (3)	C(7)	-0.02 (5)	H(5)	0.11 (3)
N(1)	-0.04 (5)	C(8)	-0.14 (6)	H(6)	0.19 (3)
N(2)	0.02 (5)	C(9)	-0.09 (5)	H(7)	0.13 (2)
N(3)	0.14 (5)	C(10)	-0.16 (5)	H(8A)	-0.05 (3)
N(4)	0.07 (5)	C(11)	-0.03 (5)	H(8B)	0.10 (3)
C(1)	-0.08 (5)	C(12)	-0.24 (5)	H(8C)	0.10 (3)
C(2)	-0.09 (5)	C(13)	-0.24 (6)	H(11)	0.16 (3)
C(3)	-0.25 (5)	H(1N)	0.19 (3)	H(13)	0.17 (3)

order to confirm this conjecture, we were keen to verify that the intramolecular interaction N(1)—H(1N)···O(1) is indeed a real hydrogen bond rather than being a close contact simply due to geometric constraints. A charge-density study of MBADNP was thus conducted, since this allows one to establish whether or not a bond critical point exists within this contact, its existence and properties being definitive proof of such an interaction (Koch & Popelier, 1995; Bader, 1998; Tsirelson *et al.*, 1998). The charge-density study was also of value on two other counts, since it enabled us to (*a*) investigate the nature of the molecular polarizability in detail and (*b*) derive the solid-state value for the molecular dipole moment of MBADNP and its tensorial components. This information is very desirable, given the dependence of the NLO effect on polarizability and charge distribution.

3.2. Charge-density study of MBADNP

A summary of the multipolar refinement details for MBADNP is given in Table 4. Since the geometry is very similar to that derived from the neutron study, all bond distances and angles are deposited along with the corresponding fractional coordinates and anisotropic displacement parameters for all non-H atoms.

Residual density maps of the molecule, given in Fig. 6, show featureless regions of little residual electron density, indicating that the electron distribution is well described by the multipole model. The rigid-bond test, which was applied to all bonds not involving H atoms during the refinement, showed that only one bond [N(1)—C(7)] has a difference in mean-square displacement amplitudes along the bond direction (0.0013 Å^2) which slightly exceeds 0.001 Å^2, thus failing to satisfy the test criterion. The cause for this is unknown, but it is probably not significant since the value is only about one tenth of the actual values for the corresponding thermal parameters.

3.2.1. Modelling of molecular charge transfer. Since an electroneutrality constraint is applied over the whole asymmetric unit, the extent of charge transfer ensuing in the molecule can be derived wholly from the monopole populations. The charge on a given atom is the difference between the monopole population for this atom, as observed from the charge-density study, and the number of valence electrons classically present in the atom, *e.g.* for a C atom, the monopole population would be four in the absence of any charge

transfer. The charges present on each atom in MBADNP are given in Table 5.

All values of the derived charges conform to simple electronegativity expectations. The charge is concentrated in two areas: the phenyl ring and the pyridine ring. The respective pseudoatom charges of the branch atoms C(7) and N(1) are very small compared with those for atoms in each ring. Therefore, the two areas of charge transfer are localized in each ring. This validates our previous assumption about the charge-transfer axis when calculating the phase-matching angle of MBADNP (see Cole *et al.*, 1997). The charge on O(1) is significantly larger than that for all other O atoms that comprise the nitro groups. Given that O(1) is the hydrogen-bond acceptor for the aforementioned short intramolecular contact N(1)—H(1N)···O(1), this significantly greater electronegativity lends direct evidence to its existence. The pseudoatomic charge on O(4) is also notable compared with that on O(1) and O(2). This presumably arises from the fact that O(4) is the hydrogen-bond acceptor for the only classical (N, O, F donors) intermolecular hydrogen bond in this compound, whose electrostatics are reflected in this value. The effect is not as marked as for O(1), presumably because this intermolecular interaction is much weaker than the intramolecular hydrogen bond.

3.2.2. Topological analysis of electronic structure. Electron deformation density (EDD) maps of the molecule, ρ-ρ_{IAM}, which effectively represent the valence density, are given in Fig. 7. These maps illustrate the nature and extent of the polarization ensuing in the molecule. All critical points, Laplacian ($\nabla^2\rho$) values and ellipticity (ε) values found within the molecule are given in Tables 6 and 7. Bond $(3,-1)$ critical points indicate the point of minimum electron density along the bond path joining two specified atoms. Owing to the nature of bonding, one of these points must always exist between any bond. Ring $(3,+1)$ critical points occur where two perpendicular local minima are present, *i.e.* in the centre of the plane of a ring. Laplacian values represent a local concentration (negative) or depletion (positive) of electronic charge at a given point. Ellipticity values refer to the extent of asymmetry about the cross section of the centre of a bond, *e.g.* $\varepsilon = 0$ for a pure σ-bond since the cross section of its centre is circular. See Bader (1994) for a more comprehensive discussion of these topological parameters.

The electron density in each bond of the pyridine ring is distributed essentially equally between the bonding atoms, thus indicating that there is no polarization within the ring. The critical points existing almost at the mid-points between the bonds C(9)—C(10), C(10)—C(11), C(11)—C(12) and C(12)—C(13) confirm this. The critical points of the bonds N(2)—C(9) and N(2)—C(13) are displaced from the bond-distance mid-point towards the C atom in both cases. This simply reflects the greater contribution of electron density to the bond from the more electronegative N atom. The ring is delocalized with the N atom contributing electron density (in a p-orbital perpendicular to the plane shown in Fig. 7d) to the ring in order to satisfy Hückel's $4n + 2$ rule for aromaticity. The ellipticity values of the N(2)—C(9) and N(2)—C(13) bonds are slightly lower than the more typical values for other bonds in the ring, which reflects the slightly poorer orbital

overlap between the different elemental types. The lone pair of the N atom N(2) can be seen clearly in the plane pointing away from the ring in Fig. 7(d). A local depletion of charge is present at the centre of the ring as expected. A corresponding (3,+1) critical point was located at this centre.

The $meta$- and $para$-nitro groups show a similar valence-electron distribution to each other. In both groups, there is a larger amount of electron density present in the C—N bond than one would expect from a σ-bond. An examination of the relevant C—N ellipticity values reveals that there is a significant amount of π-bonding present in this bond. Thus, the N out-of-plane p-orbital must be involved in conjugation with the ring. The concentration of charge in this bond causes a corresponding depletion of charge in the N—O bonds that would normally be delocalized. Therefore, the ellipticity values for the N—O bonds are more typical of a single bond
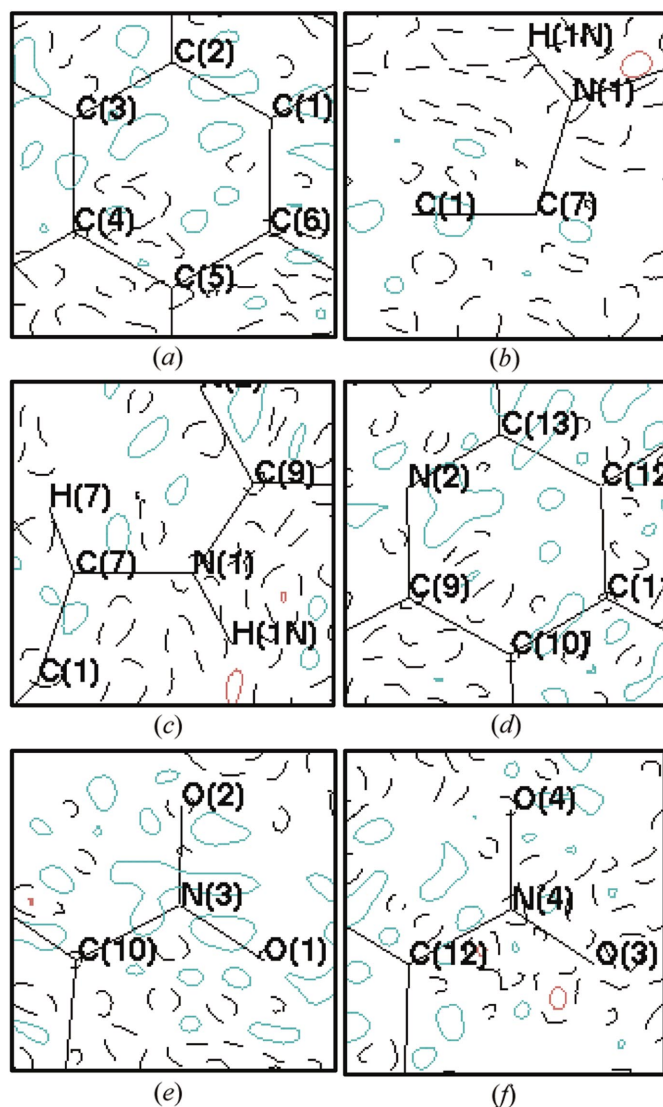
Figure 6
Residual density maps of the (a) phenyl, (b) C(1) to N(1), (c) C(7) to C(9), (d) pyridine, (e) $meta$-nitro and (f) $para$-nitro groups in MBADNP out to $\sin\theta/\lambda = 0.7$ Å^{-1}, with contour levels of 0.1 e Å^{-3} (blue lines are positive, red lines are negative, black lines are zero).
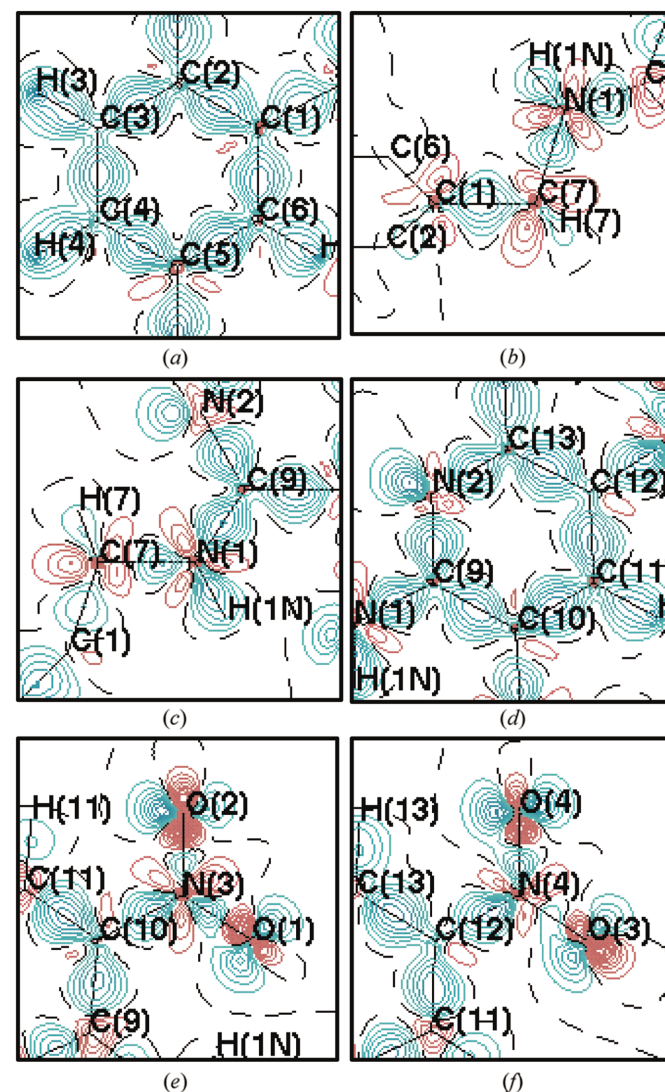
Figure 7
Model electron deformation density maps of the (a) phenyl, (b) C(1) to N(1), (c) C(7) to C(9), (d) pyridine, (e) $meta$-nitro and (f) $para$-nitro groups in MBADNP, with contour levels of 0.1 e Å^{-3} (blue lines are positive, red lines are negative, black lines are zero).

Table 6
Parameters (e Å^{-5}, e Å^{-3}, Å) of all (3, −1) bond critical points located within the molecule MBADNP.

λ_1, λ_2 and λ_3 represent the second derivative of the electron density, ρ, in each orthogonal direction; $\nabla^2\rho$ is the Laplacian (the sum of these λ_n eigenvalues); ε is the ellipticity of the bond; R_{ij} is the length of the bond path between the atoms; $d1$ and $d2$ represent the distance between the first and second atoms specified in the bond column and the critical point, respectively.

Bond	λ_1	λ_2	λ_3	ρ	$\nabla^2\rho$	ε	R_{ij}	$d1$	$d2$
O(1)—N(3)	−29.5	−25.9	48.2	3.18	−7.3	0.14	1.24	0.630	0.609
O(1)—H(1N)	−0.8	−0.7	4.3	0.19	2.8	0.21	2.00	1.209	0.787
O(2)—N(3)	−28.0	−25.9	45.3	3.11	−8.6	0.08	1.23	0.628	0.600
O(3)—N(4)	−26.8	−25.0	43.7	3.06	−8.0	0.07	1.23	0.666	0.568
O(4)—N(4)	−28.2	−27.2	48.4	3.20	−7.0	0.04	1.24	0.633	0.603
N(1)—C(7)	−9.9	−9.2	7.3	1.57	−11.9	0.08	1.47	0.908	0.564
N(1)—C(9)	−20.3	−18.0	9.5	2.41	−28.8	0.13	1.34	0.788	0.550
N(1)—H(1N)	−27.0	−25.7	30.5	2.05	−22.2	0.05	1.02	0.769	0.246
N(2)—C(9)	−18.4	−16.5	14.4	2.31	−20.5	0.11	1.36	0.750	0.610
N(2)—C(13)	−19.7	−18.4	10.9	2.44	−27.1	0.07	1.32	0.760	0.562
N(3)—C(10)	−13.1	−10.4	10.2	1.78	−13.3	0.27	1.45	0.873	0.581
N(4)—C(12)	−14.0	−10.9	11.5	1.87	−13.4	0.28	1.45	0.858	0.588
C(1)—C(2)	−15.6	−13.1	10.1	2.12	−18.6	0.19	1.40	0.697	0.702
C(1)—C(6)	−14.9	−12.6	9.2	2.03	−18.3	0.18	1.40	0.660	0.744
C(1)—C(7)	−11.1	−11.0	10.5	1.68	−11.7	0.01	1.52	0.770	0.754
C(2)—C(3)	−16.1	−13.6	9.4	2.11	−20.3	0.18	1.40	0.694	0.705
C(2)—H(2)	−16.3	−15.3	14.2	1.75	−17.3	0.06	1.09	0.715	0.372
C(3)—C(4)	−15.4	−13.2	9.1	2.08	−19.5	0.16	1.39	0.699	0.695
C(3)—H(3)	−16.9	−15.7	19.3	1.75	−13.4	0.08	1.09	0.748	0.340
C(4)—C(5)	−15.8	−13.1	9.4	2.08	−19.5	0.21	1.40	0.668	0.733
C(4)—H(4)	−15.9	−15.4	18.9	1.67	−12.4	0.03	1.09	0.755	0.338
C(5)—C(6)	−16.7	−14.2	9.3	2.16	−21.6	0.17	1.39	0.684	0.709
C(5)—H(5)	−15.8	−14.6	13.0	1.72	−17.5	0.08	1.08	0.688	0.397
C(6)—H(6)	−16.1	−15.6	14.5	1.72	−17.2	0.03	1.09	0.722	0.365
C(7)—C(8)	−10.2	−9.8	10.0	1.59	−10.0	0.04	1.53	0.801	0.728
C(7)—H(7)	−15.5	−15.1	15.9	1.72	−14.8	0.02	1.10	0.734	0.367
C(8)—H(8A)	−13.6	−12.9	13.9	1.67	−12.6	0.05	1.09	0.672	0.421
C(8)—H(8B)	−15.4	−15.0	15.5	1.73	−14.9	0.03	1.10	0.721	0.376
C(8)—H(8C)	−15.0	−14.6	15.5	1.70	−14.1	0.03	1.09	0.722	0.373
C(9)—C(10)	−14.5	−12.2	10.0	1.95	−16.7	0.18	1.44	0.703	0.734
C(10)—C(11)	−16.9	−14.2	9.4	2.21	−21.7	0.19	1.38	0.707	0.675
C(11)—C(12)	−15.9	−13.2	9.2	2.13	−19.9	0.20	1.39	0.723	0.663
C(11)—H(11)	−16.9	−16.2	15.9	1.77	−17.2	0.04	1.09	0.735	0.353
C(12)—C(13)	−15.6	−13.2	9.9	2.13	−19.0	0.18	1.40	0.681	0.720
C(13)—H(13)	−16.8	−15.9	16.0	1.77	−16.7	0.06	1.09	0.733	0.353

Table 7
Parameters (e Å^{-5}, e Å^{-3}, Å) of all (3,+1) ring critical points located within the molecule of MBADNP.

λ_1, λ_2 and λ_3 represent the second derivative of the electron density, ρ, in each orthogonal direction; $\nabla^2\rho$ is the Laplacian (the sum of these λ_n eigenvalues).

Distance between critical point and atom X						λ_1	λ_2	λ_3	ρ	$\nabla^2\rho$
C(1)	C(2)	C(3)	C(4)	C(5)	C(6)					
1.404	1.392	1.399	1.411	1.398	1.384	−0.5	1.8	1.9	0.22	3.2
C(9)	C(10)	C(11)	C(12)	C(13)	N(2)					
1.361	1.343	1.402	1.393	1.382	1.408	−0.6	2.0	2.1	0.24	3.4
C(9)	C(10)	N(3)	O(1)	H(1 N)	N(1)					
1.521	1.555	1.550	1.365	1.139	1.446	−0.4	0.7	1.8	0.14	2.1

than of a double bond. There is slightly more charge transfer from the O—N bonds to the N—C bond in the *para* group than the *meta* group, judging by the ellipticity values. The less well developed positive lobes on the N atom in the *para* group compared with those in the *meta* group in the EDD maps also reflect this. As a result of this conjugation, the C—N bond is slightly polarized towards the C atom as is evident from the

relevant EDD maps and the relevant pseudo-atomic charges (see Table 5). The two lone pairs on each O atom can be seen clearly in the EDD maps (Figs. 7e and 7f).

The ellipticity value for the N(1)—C(9) bond suggests that the N(1) atom may be partially conjugated to the pyridine ring. Other than this, only σ-bonding is present in the bridge between the two rings, judging by the relevant ellipticity values. Hence, in principle, there should be free rotation about the N(1)—C(7) bond. However, as we saw earlier, an intramolecular hydrogen bond, N(1)—H(1N)···O(1), appears to restrict such freedom. A bond critical point relating to this hydrogen bond was located (see Table 6), proving that this intramolecular bond exists. The EDD map, given in Fig. 8(a), illustrates the O-lone-pair directionality towards the H atom, and the Laplacian map in Fig. 8(b) shows the local depletion of charge, near to the H atom and along the H(1N)···O(1) bond direction, that one would expect for a hydrogen bond, since such an H atom would be very acidic. This Laplacian map also shows local charge depletion near the centre of the ring that is made by the formation of this hydrogen bond. A corresponding (3,+1) ring critical point relating to this depletion in charge was found here (see Table 7). No (3,−1) critical points were found for any of the other four possible intramolecular non-bonded contacts suggested by the X-ray and neutron structural results. Therefore, we presume that these close contacts result simply from the physical geometrical restrictions imposed within the molecule, rather than from electrostatic interactions. The methyl group, which is bonded to the C(7) atom in the bridge and lies out of the overall plane of the molecule, shows no special features.

All bond critical points in the phenyl ring lie close to the bond mid-point, thus indicating that there is no electronic polarization present here. Ellipticity values all lie between 0.15 and 0.21 (mean value 0.18), which shows that the ring electron density is fairly uniformly delocalized. The values are slightly lower than those obtained from the *ab initio* (Bader *et al.*, 1983) and *XD* refinements (Goeta & Lehmann, 1994) of benzene [*ab initio*, 0.23 for all bonds; *XD* refinement, 0.28/0.22/0.19 (mean value 0.23)]. The involvement of the phenyl C atoms [all but the bridging C(1)] and their associated H atoms in intermolecular hydrogen bonding, and the slight perturbation of the ring current due to the presence of a bridging unit compared with the isolated ring, are presumably responsible for this difference. All adjoining H atoms are polarized towards the C atoms to which they are bonded, as expected. A local depletion of charge is present at the centre of the ring,

and a corresponding (3,+1) critical point was located. The level of this charge depletion is approximately the same as that determined at the centre of the pyridine ring.

In summary, the transfer of charge appears to be concentrated around the pyridine ring, its NH and NO$_2$ substituents invoking the 'push–pull' effect, respectively, and the pyridine ring itself acting as a good (null-polarized) electronic medium through which charge can be transferred. The *para* contribution to charge transfer across the ring is greater than the *meta* contribution, as one would expect. However, the *meta*-nitro group is crucial to the formation of the intramolecular hydrogen bond that effects the twist of the two rings with respect to each other. Whilst the phenyl group shows negligible polarization within itself and therefore is a good medium for the propagation of charge-transfer processes, the σ-bonding observed in the bridge effectively isolates this moiety from the charge transfer ensuing in the rest of the molecule. One can therefore conclude that the phenyl ring influences the NLO effect mostly by being a neutral spacer to control the packing effects previously discussed, whilst the pyridine moiety is host to the principal charge-transfer effect that ensues.

3.2.3. Calculation of the solid-state dipole moment and its principal coefficients. Whilst charge-density methods will never override the more standard techniques used for calculating the dipole moments of a molecule, it should be pointed out that charge-density analyses yield tensorial values of moments, whereas most standard techniques provide just one overall magnitude of the moment. Moreover, charge-density analyses are derived from solid-state results, whereas all other techniques are based on liquid or gaseous phases. Given that the SHG effect in these materials results from the solid state, the direct evaluation of the dipole moment in the same phase is paramount in this investigation, since this illustrates the level and direction of charge-transfer ensuing across the molecule. Moreover, the deduction of its individual tensorial components enables the charge-transfer axis to be derived explicitly.

Multipolar moments obtained from charge-density analyses very strongly depend on the method of space partitioning and the choice of origin used. In this paper, the dipolar values are derived from the pseudoatom space partitioning model, a Cartesian frame of reference was used and the centre of mass was taken to be the origin. For a more comprehensive review of molecular electrostatic moments from X-ray diffraction, see Spackman (1992). The coefficients of the dipole moment determined in this study are $p_x = -1.03 \times 10^{-30}$ Cm (-3.1 Debye), $p_y = 8.34 \times 10^{-30}$ Cm (2.5 Debye) and $p_z = 1.30 \times 10^{-29}$ Cm (3.9 Debye), thus yielding an overall magnitude of 1.87×10^{-29} Cm (5.6 Debye).

The overall value of this dipole moment is moderately large compared with those determined for various molecules by Spackman (1992). This is expected since MBADNP possesses several strong donor and acceptor groups at opposing sides of the pyridyl group, and thereby presents significant polarizability. The dipole moment projects from the molecular centre of mass along a vector that intersects the two nitro groups. This directionality conforms with that assumed for the charge-transfer axis reported by Cole *et al.* (1997), which was based on a simplistic method of resolving δ^+ and δ^- forces across the molecule that were assumed to be equally strong, *i.e.* only taking into account the sense of the electrostatics, not the magnitude.

4. Concluding remarks

This study illustrates the importance of intramolecular hydrogen bonding and its effects on the three-dimensional packing arrangement of a molecule. More generally, the nature of hydrogen bonding, which commonly dictates the packing arrangement within a crystal lattice for good organic NLO active compounds, cannot be predicted reliably. However, the analysis of these interactions can rationalize apparent discrepancies between related NLO active compounds. The charge-density study on MBADNP confirms the existence of the strong intramolecular interaction that
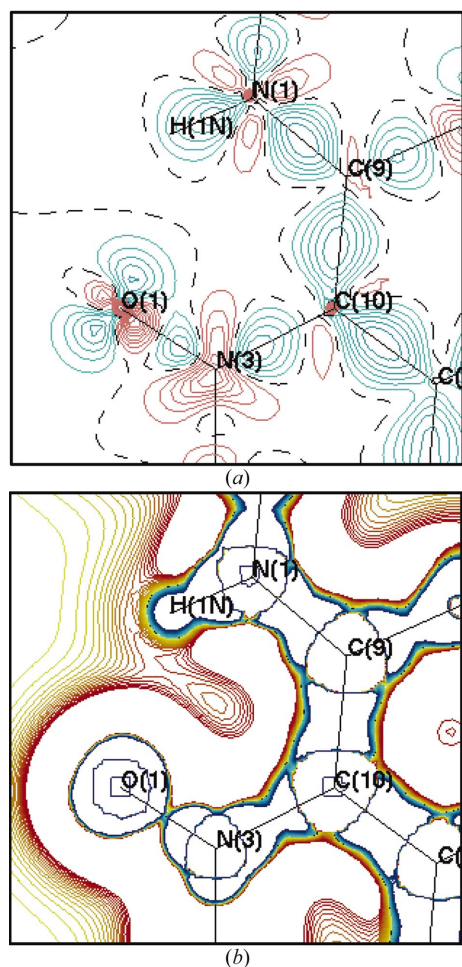
Figure 8
(*a*) Model electron deformation density and (*b*) Laplacian maps showing the intramolecular hydrogen bond N(1)—H(1N)$\cdots$O(1) in MBADNP, with contour levels of 0.1 e Å^{-3} and 0.2 e Å^{-5}, respectively (blue lines are positive, red lines are negative, black lines are zero).

causes its less favourable crystal packing compared with that of MBANP.

The analysis of the nature of the polarization of electron density in MBADNP shows that it is the pyridine group that acts as the medium for charge-transfer processes, these being controlled by its direct substituents. This finding is corroborated by the fact that the dipole moment deduced by this charge-density study lies along the same direction as that assumed for the charge-transfer axis – which was derived without taking into account the phenyl group (Cole *et al.*, 1997). Given that charge transfer underpins the SHG effect on a molecular scale, further attempts to engineer a strongly SHG-active derivative of MBANP will concentrate on this part of the molecule.

References

Albrecht, A. C. & Morell, A. (1979). *Chem. Phys. Lett.* **64**, 46–50.
Archer, J. M. & Lehmann, M. S. (1986). *J. Appl. Cryst.* **19**, 456–458.
Armstrong, J. A., Bloembergen, N., Ducuing, J. & Pershan, P. S. (1962). *Phys. Rev. B*, **127**, 1918–1939.
Bader, R. F. W. (1994). *Atoms in Molecules. A Quantum Theory.* Oxford: Clarendon Press.
Bader, R. F. W. (1998). *J. Phys. Chem.* A**102**, 7314–7323.
Bader, R. F. W., Slee, T. S., Cremer, D. & Kraka, E. (1983). *J. Am. Chem. Soc.* **105**, 5061–5068.
Bailey, R. T., Bourhill, G., Cruickshank, F. R., Pugh, D., Sherwood, J. N., Simpson, G. S. & Wilkie, S. (1993). *Mol. Cryst. Liq. Cryst.* **231**, 223–229.
Bailey, R. T., Cruickshank, F. R., Pavlides, P., Pugh, D. & Sherwood, J. N. (1991). *J. Phys. D*, **24**, 135–145.
Barthelemy, A. (1984). *MAD.* ILL Technical Report, 84BAIST. Institut Laue Langevin, Grenoble, France.
Blessing, R. H. (1986). *J. Appl. Cryst.* **19**, 412.
Blessing, R. H. (1995). *Acta Cryst.* B**51**, 816–823.
Burland, D. M. (1994). *Chem. Rev.* **94**, 1–2.
Burland, D. M., Miller, R. D. & Walsh, A. (1994). *Chem. Rev.* **94**, 31–76.
Cady, W. G. (1946). *Piezoelectricity.* New York: McGraw-Hill.
Chemla, D. S. & Zyss, J. (1987). *Nonlinear Optical Properties of Organic Molecules and Crystals*, Vol. 1. Orlando: Academic Press.
Cheng, L., Gorman, C. B., Marder, S. R. & Tiemann, B. G. (1993). *Proc. SPIE*, **1775**, 19–31.
Cheng, L.-T., Tam, W., Marder, S. R., Stiegman, A. E., Rikken, G. & Spangler, C. W. (1991). *J. Phys. Chem.* **95**, 10643–10652.
Clementi, E. & Raimondi, D. L. (1963). *J. Chem. Phys.* **63**, 2686–2689.
Cole, J. M. (1997). PhD thesis, University of Durham, England.
Cole, J. M., Howard, J. A. K. & MacBride, J. A. H. (1997). *Acta Cryst.* C**53**, 1331–1334.
Cole, J. M., McIntyre, G. J. & Howard, J. A. K. (2001). *Acta Cryst.* B**57**, 410–414.
Copley, R. C. B., Goeta, A. E., Lehmann, C. W., Cole, J. C., Yufit, D. S., Howard, J. A. K. & Archer, J. M. (1997). *J. Appl. Cryst.* **30**, 413–417.
Coppens, P., Leiserowitz, L. & Rabinovich, D. (1965). *Acta Cryst.* **18**, 1035–1038.
Davydov, B. L., Derkacheva, L. D., Dunina, V. V., Koreneva, L. G., Samokhina, M. A., Zhabotinskii, M. E. & Zolin, V. F. (1970). *Zh. Eksp. Teor. Fiz. Pis'ma Red.* **12**, 24–26.
Docherty, V. J., Pugh, D. & Morley, J. O. (1985). *J. Chem. Soc. Faraday Trans. 2*, **81**, 1179–1192.
El Haouzi, A., Hansen, N. K., Le Henaff, C. & Protas, J. (1996). *Acta Cryst.* A**52**, 291–301.
Fejer, M. M. (1994). *Phys. Today*, pp. 25–57.
Franken, P. A. & Ward, J. F. (1963). *Rev. Mod. Phys.* **35**, 23–39.
Goeta, A. E. & Lehmann, C. W. (1994). Communication to the British Crystallographic Association Annual Spring Meeting, Newcastle, England.
Gorman, C. B. & Marder, S. R. (1993). *Proc. Natl Acad. Sci. USA*, **90**, 11297–11301.
Hansen, N. K. & Coppens, P. (1978). *Acta Cryst.* A**34**, 909–921.
Jen, A. K.-Y., Rao, V. P., Wong, K. Y. & Drost, K. J. (1993). *J. Chem. Soc. Chem. Commun.* pp. 90–92.
Koch, U. & Popelier, P. L. A. (1995). *J. Phys. Chem.* **99**, 9747–9754.
Kondo, T., Morita, R., Ogasawara, N., Umegaki, S. & Ito, R. (1989). *Jpn. J. Appl. Phys.* **28**, 1622–1628.
Kondo, T., Ogasawara, N., Ito, R., Ishida, K., Tanase, T., Murata, T. & Hidai, M. (1988). *Acta Cryst.* C**44**, 102–104.
Koritsanszky, T., Howard, S., Richter, T., Mallinson, P., Su, Z. & Hansen, N. (1994). *XD. A Computer Program Package for Multipole Refinement and Analysis of Charge Densities from Diffraction Data.* Berlin, Cardiff, Glasgow, Buffalo, Nancy.
Lalama, S. J. & Garito, A. F. (1979). *Phys. Rev. A*, **20**, 1179–1194.
Lehmann, M. S. & Wilson, S. (1987). *COLL5N. College V Data Reduction System, Treatment of Reflection Profiles.* Institut Laue Langevin, Grenoble, France.
Long, N. J. (1995). *Angew. Chem. Int. Ed. Engl.* **34**, 21–38.
Marder, S. R. & Perry, W. (1993). *Adv. Mater.* **5**, 804–815.
Oudar, J. L. (1977). *J. Chem. Phys.* **67**, 446–457.
Oudar, J. L. & Zyss, J. (1982). *Phys. Rev. A*, **26**, 2028–2048.
Sarma, J. A. R. P., Allen, F. H., Hoy, V. J., Howard, J. A. K., Thaimattam, R., Biradha, K. & Desiraju, G. R. (1997). *J. Chem. Soc. Chem. Commun.* pp. 101–102.
Sheldrick, G. M. (1990). *Acta Cryst.* A**46**, 467–473.
Sheldrick, G. M. (1993). *SHELXL*93. University of Göttingen, Germany.
Sheldrick, G. M. (1997). *SHELXL*97. University of Göttingen, Germany.
Spackman, M. A. (1992). *Chem. Rev.* **92**, 1769–1797.
Stewart, R. F. (1977). *Isr. J. Chem.* **16**, 124–131.
Stewart, R. F., Davidson, E. R. & Simpson, W. T. (1965). *J. Chem. Phys.* **42**, 3175–3187.
Terpstra, M., Craven, B. M. & Stewart, R. F. (1993). *Acta Cryst.* A**49**, 685–692.
Tsirelson, V., Abramov, Y., Zavodnik, V., Stash, A., Belokoneva, E., Stahn, J., Pietsch, U. & Feil, D. (1998). *Struct. Chem.* **9**, 249–254.
Twieg, R. J., Azema, A., Jain, K. & Cheng, Y. Y. (1982). *Chem. Phys. Lett.* **92**, 208–211.
Twieg, R. J. & Dirk, C. W. (1986). IBM Research Report RJ 5237 (54077). IBM, San Jose, California, USA.
Volkov, A., Abramov, Y. A. & Coppens, P. (2001). *Acta Cryst.* A**57**, 272–282.
Wilkinson, C., Khamis, H. W., Stansfield, R. F. D. & McIntyre, G. J. (1988). *J. Appl. Cryst.* **21**, 471–478.
Zyss, J. (1994). Editor. *Molecular Nonlinear Optics: Materials, Physics and Devices.* San Diego: Academic Press.